Natural Resources
Canada

Ressources naturelles
Canada

GEOMATICS CANADA
OPEN FILE 67

# SAR interferometry with the RADARSAT Constellation Mission

**J.P. Dudley and S.V. Samsonov**

**2022**

Canada

**GEOMATICS CANADA**
**OPEN FILE 67**


# SAR interferometry with the RADARSAT Constellation Mission


**J.P. Dudley and S.V. Samsonov**


**2022**

Publications in this series have not been edited; they are released as submitted by the author.

# Abstract

The RADARSAT Constellation Mission (RCM) is Canada's latest system of C-band Synthetic Aperture Radar (SAR) Earth observation satellites. The system of three satellites, spaced equally in a common orbit, allows for a rapid four-day repeat interval. The RCM has been designed with a selection of stripmap, spotlight, and ScanSAR beam modes which offer varied combinations of spatial resolution and coverage. Using Differential Interferometric Synthetic Aperture Radar (DInSAR) techniques, the growing archive of SAR data gathered by RCM can be used for change detection and ground deformation monitoring for diverse applications in Canada and around the world. In partnership with the Canadian Space Agency (CSA), the Canada Centre for Mapping and Earth Observation (CCMEO) has developed an automated system for generating standard and advanced deformation products and change detection from SAR data acquired by RCM and RADARSAT-2 satellites using DInSAR processing methodology. Using this system, this paper investigates four key interferometric properties of the RCM system which were not available on the RADARSAT-1 or RADARSAT-2 missions: The impact of the high temporal resolution of the four-day repeat cycle of the RCM on temporal decorrelation trends is tested and fitted against simple temporal decay models. The effect of the normalization and the precision of the radiometric calibration on interferometric spatial coherence is investigated. The performance of the RCM ScanSAR mode for wide area interferometric analysis is tested. The performance of the novel RCM Compact-polarization (CP) mode for interferometric analysis is also investigated.

# Contents

# 1. Introduction

With the successful launch of the RADARSAT Constellation Mission (RCM) on June 12th, 2019 aboard the SpaceX Falcon 9 rocket, Canada has entered into a new era of remote sensing with Synthetic Aperture Radar (SAR) (Canadian Space Agency, 2019). RCM is Canada's latest generation of Earth observation SAR satellites. The constellation of three C-band (5.55 cm wavelength) sensors offers numerous advancements in remote sensing including a rapid 4-day exact repeat revisit interval, multi-polarization capability including the Compact-polarization (CP) mode, configurable radiometric normalization of images, and wide area monitoring with Scanning Synthetic Aperture Radar (ScanSAR) (MDA Systems Ltd 2020; Thompson 2010). In this technical note, we investigate four aspects of the RCM system and address their impacts on Differential Interferometric SAR (DInSAR) analysis. We test and quantify the temporal decay properties of spatial coherence with respect to the 4-day revisit cycle of the RCM system. We examine the effects of the SAR radiometric calibrations offered by RCM on spatial coherence. The interferometric performance of RCM's ScanSAR modes for wide area monitoring are investigated as is the performance of the novel CP modes for performing interferometric analysis.

One of the key assets of the RCM system is the increased temporal resolution offered by its 4-day revisit cycle. The RCM constellation consists of three satellites in a single orbital plane with a mean altitude of 593 km and separated by 120° (Thompson 2015). Each satellite has a 12-day repeat cycle resulting in a combined 4-day repeat cycle for the constellation. This can be contrasted against other C-band sensors such as the previous generation RADARSAT-2 system which consists of a single satellite with a mean orbit of 798 km and a repeat pass interval of 24 days, as well as the Sentinel-1 system which consists of two satellites with mean orbits of 693 km with individual repeat pass intervals of 12 days and a combined repeat pass interval of 6 days (Berger et al. 2012; Davidson et al. 2010; Livingstone et al. 2006; Morena et al. 2004).

Following the relatively recent commissioning of RCM, results from DInSAR analysis of RCM data have started to emerge. High resolution RCM imagery using multiple beam modes was used on an emergency basis to monitor slope stability of Turtle Mountain in Alberta, Canada using DInSAR analysis (Lehrbass et al. 2021). RCM data was also used in a multi-sensor DInSAR ground deformation analysis of landslides in British Columbia, Canada (Huntley et al. 2021). The use of RCM for monitoring ground deformation in the Alberta oil sands has also been investigated using simulated datasets (Samsonov et al. 2015).

More generally, DInSAR techniques have been demonstrated to provide a scalable methodology for measuring and mapping ground deformation resulting from a wide variety of sources including earthquakes, volcanic eruptions, landslides, and mining and fluid injection and extraction (Aimaiti et al. 2017; Feng et al. 2014; Feng et al. 2016; Hamling et al. 2014; Huntley et al. 2021; Journault et al. 2017; Lundgren et al. 2015; Pearse et al. 2014; Samsonov and d'Oreye 2017; Samsonov et al. 2016; Singhroy et al. 2015). Here we will examine the interferometric performance and properties of some of the new novel features offered by RCM.

For DInSAR analysis, consecutive SAR acquisitions are separated in both the time and spatial domains, known as the temporal and spatial (perpendicular) baselines (Dudley and Samsonov

2020; Samsonov et al. 2017). Spatial (or geometric) decorrelation occurs due to the relative difference in position of the sensor between acquisitions, often expressed through the measure of the perpendicular baseline (Canaslan Çomut and Üstün 2012; Engelbrecht et al. 2014). Phase noise is incurred through changes to the scattering properties within a resolution cell as well as contributions from the topographic phase component.

Temporal decorrelation is associated with the loss of coherence in time due to changes in ground cover as well as surface deformation (Ferretti et al. 2003; Ferretti et al. 2001; Parizzi et al. 2010). The magnitude of this effect can depend upon many factors including the nature of the terrain, vegetation, and seasonal effects such as rain, snow, and ice. In general, the quality and coherence of DInSAR products are higher when both temporal and perpendicular baselines are small (Canaslan Çomut and Üstün 2012; Engelbrecht et al. 2014).

The effects of decorrelation in DInSAR analysis can be measured through calculation of the spatial coherence of differential interferograms. The spatial coherence is calculated as the absolute value of the cross-correlation between the SAR image pairs over a local window. The value of the spatial coherence ranges from zero to one with higher coherence values indicating greater phase stability and a more reliable signal. The size of the window over which coherence is calculated affects the spatial resolution and coherence estimation. Smaller windows offer increased resolution but increase the likelihood of erroneous values due to low sample size (Preiss and Stacy 2006; Touzi 1999). Larger windows decrease the likelihood of erroneous values but may underestimate coherence in heterogeneous areas. Additionally, as a measure of the absolute value of the cross-correlation, for very low values of the underlying coherence, the estimated or sample coherence is biased toward higher values (Preiss and Stacy 2006).

The loss of coherence (due to temporal decorrelation) can be especially problematic when performing DInSAR analyses over regions in Canada where significant seasonal and vegetative changes occur. During the longer (6 and 24 day) repeat intervals of the Sentinel-1 and RADARSAT-2 sensors, some regions in Canada experience a near total loss of coherence, precluding any measure of ground movement through DInSAR analysis. It will be examined whether the shorter 4-day repeat interval of RCM can reduce this decorrelation, the effects of which can be modeled by measuring the coherence decay over time.

It should be noted that for RCM data, there is an additional source of phase noise arising from the precision of the orbital state vectors. Through testing, it was found that the RCM predicted or "downlinked" orbit state vectors are insufficiently precise for use in DInSAR analysis. Since re-processed precise orbits will not be available for RCM data, it is necessary for the data to have been ordered with the more precise "definitive" orbit state vectors for DInSAR analysis.

An important step in SAR image formation is the radiometric calibration which allows for the pixel values in the SAR image to be related directly to the measured radar backscatter (Miranda and Meadows 2015; Small 2011). At image formation, the pixel values are scaled by the SAR processor using range-dependent Lookup Tables (LUTs) (MDA Systems Ltd 2020; MDA Technical Staff 2016; Miranda and Meadows 2015). These LUTs are stored with the image as metadata and allow for image data to be stored in 8-bit, 16-bit and 32-bit formats. For RADARSAT-2 8-bit and 16-bit LUTs are available, for Sentinel-1 a 16-bit LUTs is applied, and

for RCM 16-bit and 32-bit LUTs are available (Côté et al. 2019; MDA Systems Ltd 2020; MDA Technical Staff 2016; Miranda and Meadows 2015). Higher precision LUTs increase the dynamic range which can be represented with the cost of larger image file sizes (De Abreu et al. 2011). For example, the dynamic range of a 16-bit digital number is 96dB while the dynamic range for a 32-bit number is 192dB, however the 32-bit image data file size will be double that of the 16-bit image data file size. For sensors like RCM, the selection of the precision of the LUT has the potential to impact the quality of the interferometric measurement.

During processing, the LUT metadata is used to apply the radiometric scaling and relates the image pixel values to calibrated radar backscatter. When considering distributed targets, this calibration scaling is normalized with respect to a reference area (Small 2011; Small et al. 2009). The three conventional reference areas are Beta-nought, which is the radar backscatter per unit area in the slant range, Sigma-nought, the radar backscatter per unit area in the ground range, and Gamma-nought, the backscatter per unit are in the plane perpendicular to the line-of-sight (LOS) (MDA Technical Staff 2016; Miranda and Meadows 2015; Small 2011). These scalings are each available through application of the appropriate LUT. Additional LUT types are available for specific environments and applications such as ice, sea, land, and point target analysis (MDA Systems Ltd 2020). For this analysis we focus on the three common LUTs used for distributed target analysis (Beta-nought, Sigma-nought, and Gamma-nought).

With RCM the radar backscatter can be calibrated for different applications with an aim to make best use of the dynamic range of the LUT. For the Beta-nought, Sigma-nought, and Gamma-nought LUTs, RCM offers a choice of either 16-bit or 32-bit precision (Côté et al. 2019; MDA Systems Ltd 2020). For targets with high backscatter characteristics, saturation effects can lead to losses of interferometric coherence (Brisco et al. 2015; Imhoff 1995; Zhou et al. 2019). The choice of LUT is made when the image acquisition plan is submitted. Since users accessing the RCM catalogue data will generally not have a choice of LUT, we investigate the effect of the precision of the radiometric normalization for DInSAR analysis. In particular, we measure the effect of the LUTs precision on the spatial coherence and attempt to determine if there is a preferred choice for interferometric analysis of distributed scatterers.

One of RCM's new capabilities when compared with the previous RADARSAT-2 system, is the capability for interferometric ScanSAR analysis (Thompson 2010; Thompson 2015). These modes permit an increase in the range swath width, allowing for wide area ground deformation monitoring (Dabboor et al. 2019; Liang et al. 2013). The RCM ScanSAR modes are available at resolutions of 30m, 50m, and 100m with swath widths between 125km and 500km (Côté et al. 2019; MDA Systems Ltd 2020; Thompson 2015).

The ScanSAR mode divides the image into multiple subswaths which can be integrated into an image several times larger than a stripmap mode image (Bamler et al. 1999; Holzner and Bamler 2002; Thompson 2015). For RCM, up to 12 subswaths are used in some modes (Thompson 2015). Unlike the stripmap modes, ScanSAR raw data is composed of numerous smaller bursts of SAR data which must be processed together to form an image. For interferometric analysis, phase-preserving techniques across the ScanSAR bursts are necessary to form coherent interferometric data (Holzner and Bamler 2002). When used in interferometry, ScanSAR modes offer wide area monitoring for larger scale ground movement signals such as earthquakes,

landslides, and volcanic activity (Liang et al. 2013). We investigate the compatibility of the RCM ScanSAR mode for DInSAR analysis with a focus on its use in wide area monitoring of ground movement.

Another of RCM's capabilities which differs from the previous RADARSAT-2 mission is the addition of the CP mode (MDA Systems Ltd 2020; Thompson 2015). The CP mode transmits a circularly (C) polarized signal and receives on two orthogonal linear (horizontal and vertical) polarizations (H,V) (Raney 2019). The radar response of targets, and the associated backscatter signal, is generally dependent upon the transmitted and received polarization of the radar signal (Brisco et al. 2020; Cloude and Papathanassiou 1998; Raney 2019). The response of the target will depend upon its electrical and geometric properties and can alter the polarization of the returned signal.

CP data has been suggested for use in agricultural regions for both soil moisture estimation and crop identification (Charbonneau et al. 2010; McNairn et al. 2018). We investigate its use in DInSAR analysis, including an examination of the difference in observed spatial coherence between the CH and CV polarization combinations. The CP mode offers the intriguing potential to perform both polarimetric and interferometric analyses over a region using a single data set.


## 2. Data

The data used in this analysis was acquired from the RCM data archive through the Earth Observation Data Management System (EODMS) interface. The aim of the data selection was to obtain repeat pass RCM SAR data for the purposes of testing the DInSAR temporal decorrelation characteristics of the 4-day revisit interval, RCM ScanSAR data for wide area interferometric analysis, the effect of the radiometric calibration on spatial coherence, and the use the CP mode for interferometry. A total of 33 images were acquired over three regions of interest. The datasets are summarized in Table 1. The availability of larger RCM DInSAR datasets is expected to increase as RCM continues to acquire SAR data.

*Table 1: RCM SAR data used in this study, where Pol indicates the transmit/receive polarization, θ and φ are the incidence and heading angles.*

| Beam | Span | Pol | Resolution (m) | Swath (km) | θ° | φ° | SLC images |
|---|---|---|---|---|---|---|---|
| RCM 5M10 (asc) | 2020/03/04-2020/05/15 | HH | 5 | 30 | 36.6 | -14.5 | 16 |
| RCM SC30MC (desc) | 2020/03/01-2020/04/26 | HH | 30 | 125 | 38.6 | 191.6 | 12 |
| RCM 3MCP9 (desc) | 2020/06/19-2020/08/22 | CH, CV | 3 | 20 | 27.8 | 194.5 | 5 |

The first region of interest (ROI) is the Thompson River valley, an important transportation corridor in British Columbia, Canada which has previously been shown to be susceptible to landslide activity (Journault et al. 2017). We acquired 16 RCM ascending, single polarization

(HH) high resolution (5M10 mode) images with 4 day revisit cycle between the period of March 2020 and May 2020. The RCM ascending 5M10 mode has a nominal 5 m spatial resolution, a 30 km swath width, and a mean incidence angle of 36.6°. The data was multilooked by a factor of two in both range and azimuth, resulting in a pixel resolution of approximately 10 m by 6 m in range and azimuth. The average multilooked intensity (MLI) over this site is presented in Figure 2(a). For this region, six different radiometric calibrations were applied through differing LUTs. The applied LUTs are presented in Table 2.

*Table 2: Common LUT calibration types for distributed targets in the Thompson River site analysis.*

| LUT | Precision | Calibration |
|---|---|---|
| Unity-beta | 32-bit | Radar backscatter per unit area in slant range |
| Unity-sigma | 32-bit | Radar backscatter per unit area in ground range |
| Unity-gamma | 32-bit | Radar backscatter per unit area orthogonal to the direction of measurement |
| Constant-beta | 16-bit | Radar backscatter per unit area in slant range |
| Constant-sigma | 16-bit | Radar backscatter per unit area in ground range |
| Constant-gamma | 16-bit | Radar backscatter per unit area orthogonal to the direction of measurement |

The second ROI is focused over the Taal volcano in the Philippine province of Batangas. This is an active volcano with a history of 34 recorded eruptions and presents a significant danger to nearby populated regions (Bato et al. 2021; Delos Reyes et al. 2018; Morales et al. 2015). Recent studies in this region have provided measurements of ground deformation due to volcanic activities using DInSAR techniques (Bato et al. 2021; Morales et al. 2015). Twelve descending RCM ScanSAR (SC30MC mode) , single polarization (HH) images were acquired between March 2020 and April 2020. The SC30MC ScanSAR mode has a nominal 30 m resolution, a swath width of 125 km, and a mean incidence angle of 38.6°. The ScanSAR data is divided into 4 subswaths, containing a total of 79 bursts per image date. The data was multilooked by a factor of 6 in range and 2 in azimuth , resulting in a pixel resolution of approximately 45 m in both range and azimuth. Multilooking is chosen with an objective to get a square pixel on the ground. An averaged MLI for this site along with a visual representation of the spatial extents of the 79 bursts is presented in Figure 7(a).

The third region is an agricultural region south of Bassano, Alberta, Canada for which RCM CP SAR data was available.. Five RCM descending very high resolution (3MCP9 mode) images in both the CH and CV polarizations were acquired between June 2020 and August 2020. The descending 3MCP9 mode has a nominal spatial resolution of 3 m, a swath width of 20 km, and a mean incidence angle of 27.8°. The data was multilooked by a factor of two in both range and azimuth, resulting in a pixel resolution of approximately 8 m by 5 m in range and azimuth. The average MLI over this site is presented in Figure 10(a).

## 3. Methods

All RCM SAR datasets were processed using the software which forms the basis of the Government of Canada's automated processing system for change detection and ground deformation analysis (Dudley and Samsonov 2020; Samsonov et al. 2017). This software was developed under the Canadian Space Agency (CSA) Data Utilization and Application Plan (DUAP) and enables automated DInSAR processing of SAR data. The automated processing system utilizes the GAMMA remote sensing software suite (Wegmuller and Werner 1997) for DInSAR analysis and is performed using a High Performance Computing (HPC) cluster environment. The processing for each dataset proceeded along similar paths. For each dataset, direct (pairwise) coregistration was performed whereby each image is coregistered to the other image. A visual representation of the spatial and temporal baselines for each study is presented in Figure 1. The datasets were then multilooked (spatially averaged) by a factor of 2 in range and 2 in azimuth (ScanSAR data was multilooked by a factor of 6 in range) and differential interferograms are formed. To remove the topographic phase component, an Advanced Spaceborne Thermal Emission and Reflection (ASTER) Global Digital Elevation Model (GDEM) was ingested and coregistered to the reference date of each interferogram (Yamaguchi et al. 1998). The Digital Elevation Models (DEMs) used in the analyses are presented in Figure 2(b), Figure 7(b), and Figure 10(b). Atmospheric phase screens were not calculated as the analysis was not focused upon distinguishing ground deformation from atmospheric contributions. Adaptive spatial filtering was applied to the differential interferograms using a filtering function based on the local power spectral density (Goldstein and Werner 1998).
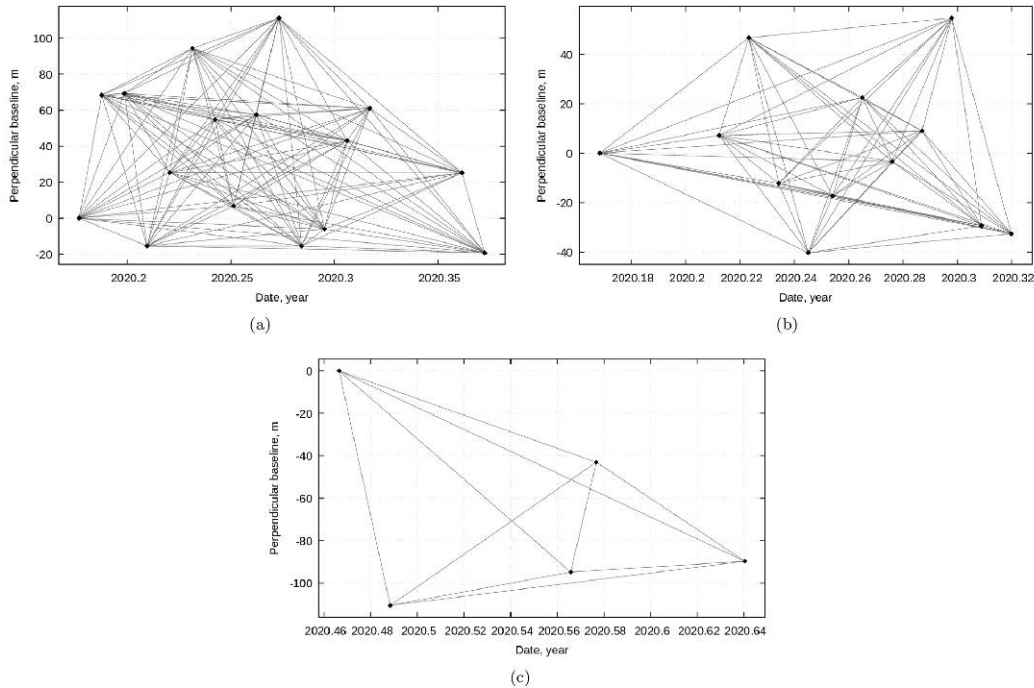


*Figure 1: Spatial and temporal baselines of RCM interferograms used in the Thompson river RCM DInSAR study (a), the RCM ScanSAR study (b), and the RCM CP study (c).*

For the adaptive filter, a filter window size of 32 pixels was used with a filtering strength of 0.4. A baseline refinement algorithm was employed to remove any residual orbital phase ramps. The spatial coherence of the differential interferograms was calculated in a 5 pixel by 5 pixel window prior to adaptive spatial filtering. The filtered interferograms are masked using a spatial coherence threshold of 0.4.

For the ScanSAR wide area ground deformation analysis, the wrapped interferograms were unwrapped using a minimum cost flow algorithm (Costantini 1998) and converted to LOS displacements. These displacements were then converted to a cumulative time series measurement using Multidimensional Small Baseline Subset (MSBAS) software through a singular value decomposition (Samsonov and d'Oreye 2017). To reduce noise, only interferograms with a mean coherence after filtering greater than a threshold of 0.65 were included in the singular value decomposition. The GAMMA software and algorithms used to process the RCM ScanSAR data can also be used to process Sentinel-1 Terrain Observation with Progressive Scan (TOPS) SAR data (Wegmuller and Werner 1997). More detailed descriptions and diagrams of this processing flow can be found in supporting documents (Dudley and Samsonov 2020; Samsonov and d'Oreye 2017).

## 4. Results

In this section, the results of the investigation into the interferometric performance of the RCM system are presented. This investigation is motivated by and focused upon four novel new features of the CRM mission: the impact of the 4-day repeat cycle on the temporal decorrelation of RCM interferograms, the effect of the precision of the radiometric calibration on spatial coherence measurements, and the performance of both the RCM ScanSAR and CP mode in interferometric analysis. The results of each study are presented in the following subsections.

## 4.1 Spatial and Temporal Decorrelation

The effects of decorrelation were tested for the Thompson River region using the RCM data listed in Table 1. Examples of the MLI, DEM, and the wrapped interferometric phase and coherence for a 4-day period are presented in Figure 2. For this test, the spatial coherence of 120 unfiltered interferograms was measured in a 5 pixel by 5 pixel window. Trends in temporal decorrelation were tested as a function of the percentile coherence as well as for specific land cover types.

In the first test, for each interferogram, the coherence was measured across the full scene at 5 percentile levels from the 50th to the 90th percentile in coherence. The percentile represents the score below which a given percentage of scores fall. For example, the 50th percentile coherence represents the median coherence value of the image, with half of all other coherence values falling beneath. Similarly, the 90th percentile coherence is the value of the coherence such that 90% of other coherence values in the image fall beneath it.
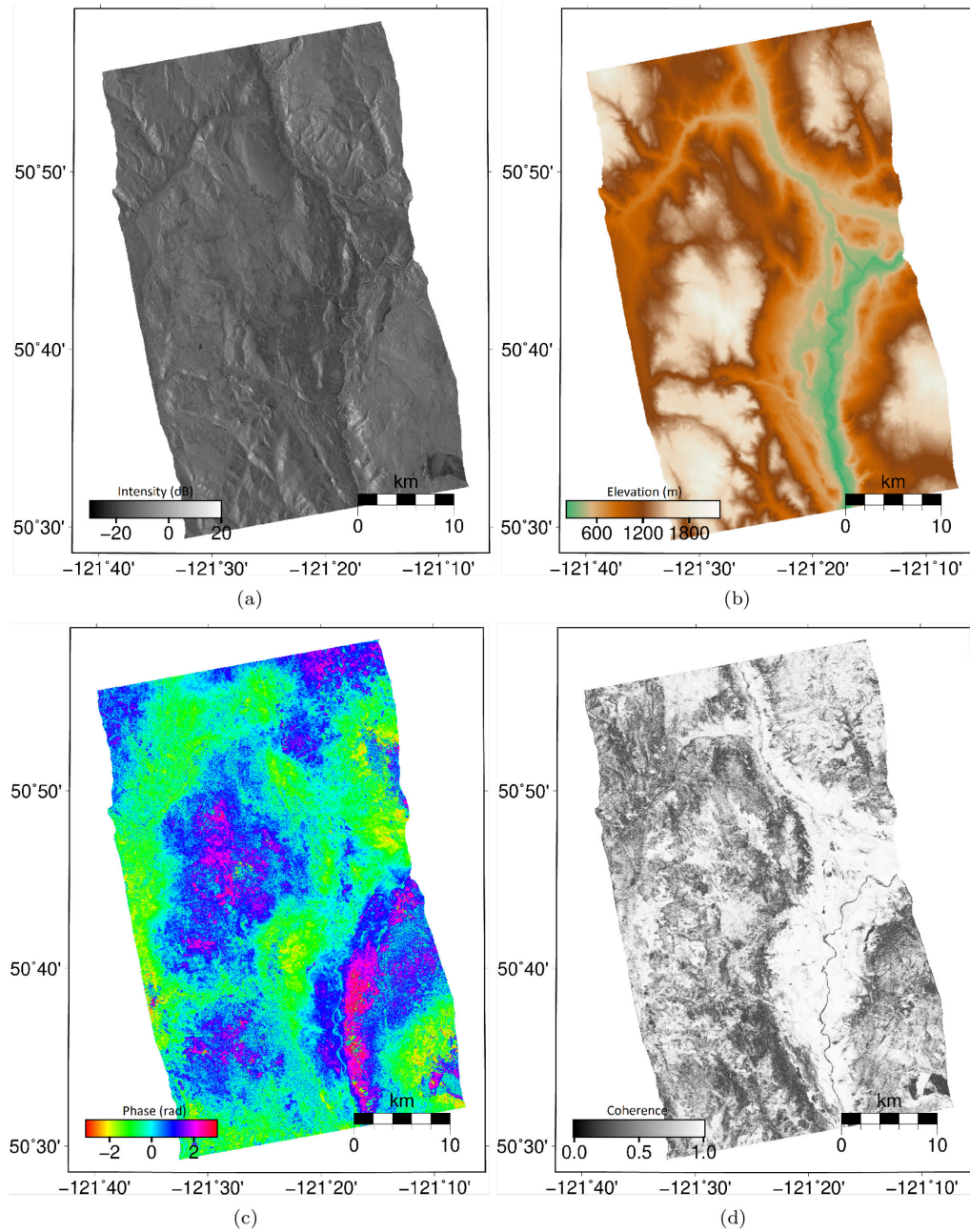
*Figure 2: Overview of the Thompson River valley analysis region. The average MLI (a) was computed from 16 RCM ascending, right-looking SAR images from 2020/03/04 to 2020/05/15. The DEM (b) over the region was obtained from the ASTER GDEM archive. The spatially filtered wrapped phase (c) and coherence (d) for a 4 day period between 2020/03/04 and 2020/03/08 shows changes in phase due to both ground movement and atmospheric delays as well as temporal decorrelation due to natural changes in ground cover.*

For the second test, coherence was measured at specific locations representing five land cover types within the region: sparse vegetation, dense vegetation, agricultural, rock face, and urban.

10

For each land cover type, the mean coherence was measured within a 5 x 5 pixel window centered upon a representative region. Visual representations of these landcover regions are presented in Figure 3.
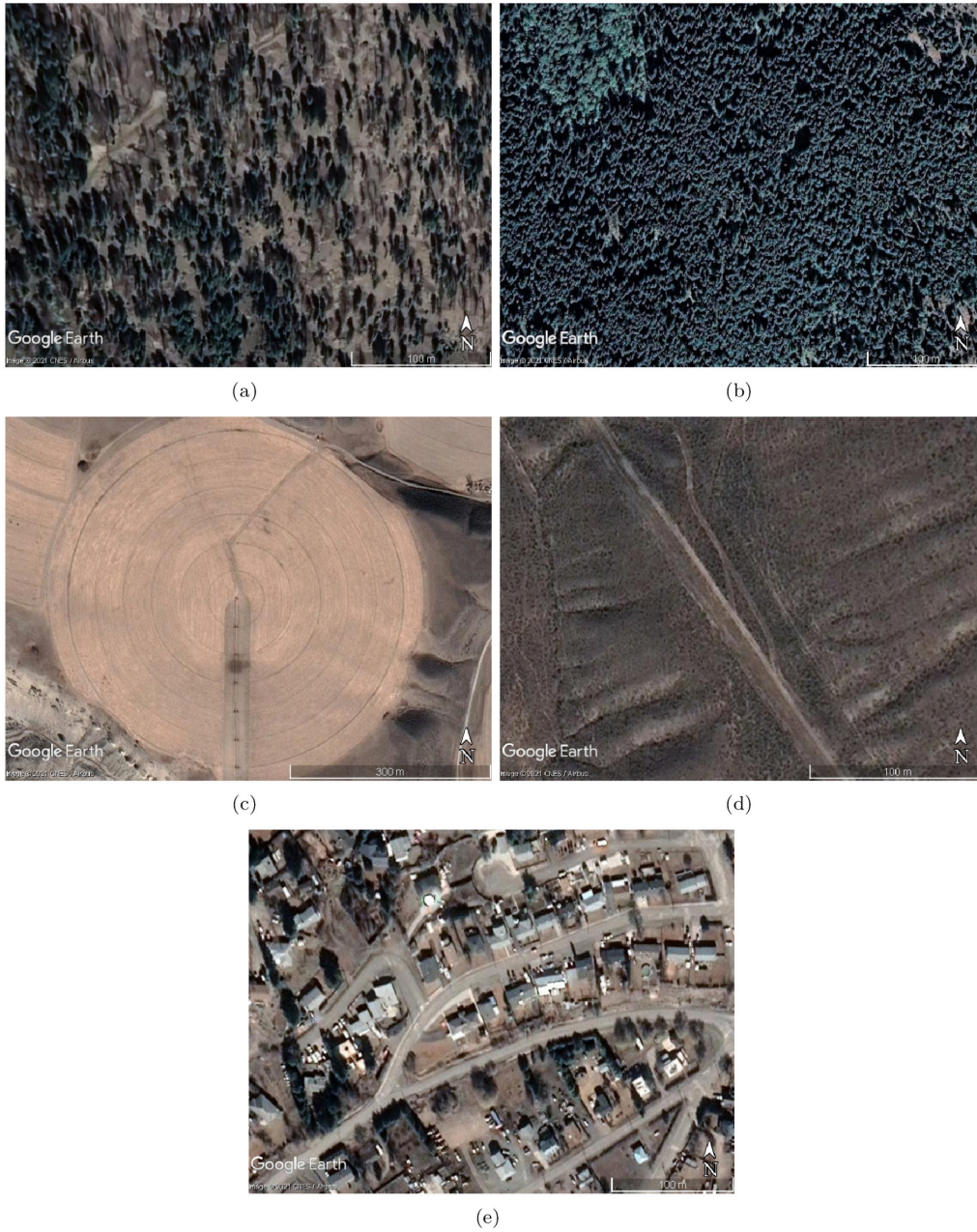


*Figure 3: Land cover types within the Thompson River monitoring region. Coherence was measure at locations with sparse vegetation (a), dense vegetation (b), agricultural activity (c), rocky terrain (d), and urban development (e). Photo credit to Google Earth.*

For both test, the interferograms were then grouped based on their temporal baselines and a simple time-dependent exponential decay model was fitted to the results for each percentile and land cover type. This decay model was designed represent the behaviour of the measured sample coherence as a function of temporal baseline separation. The exponential model asymptotes to a coherence value of one for a temporal separation of zero days (perfect coherence) and to a constant residual, non-zero coherence value ($\rho_0$) at large temporal separations:

$$\rho(t) = (1 - \rho_0)e^{\frac{-t}{\tau}} + \rho_0$$

Similar exponential decay models have been shown to have strong dependence upon land cover types (Parizzi et al. 2010). The effects of decorrelation for this test site, along with the fitted decay models are presented in Figure 4 and Figure 5.
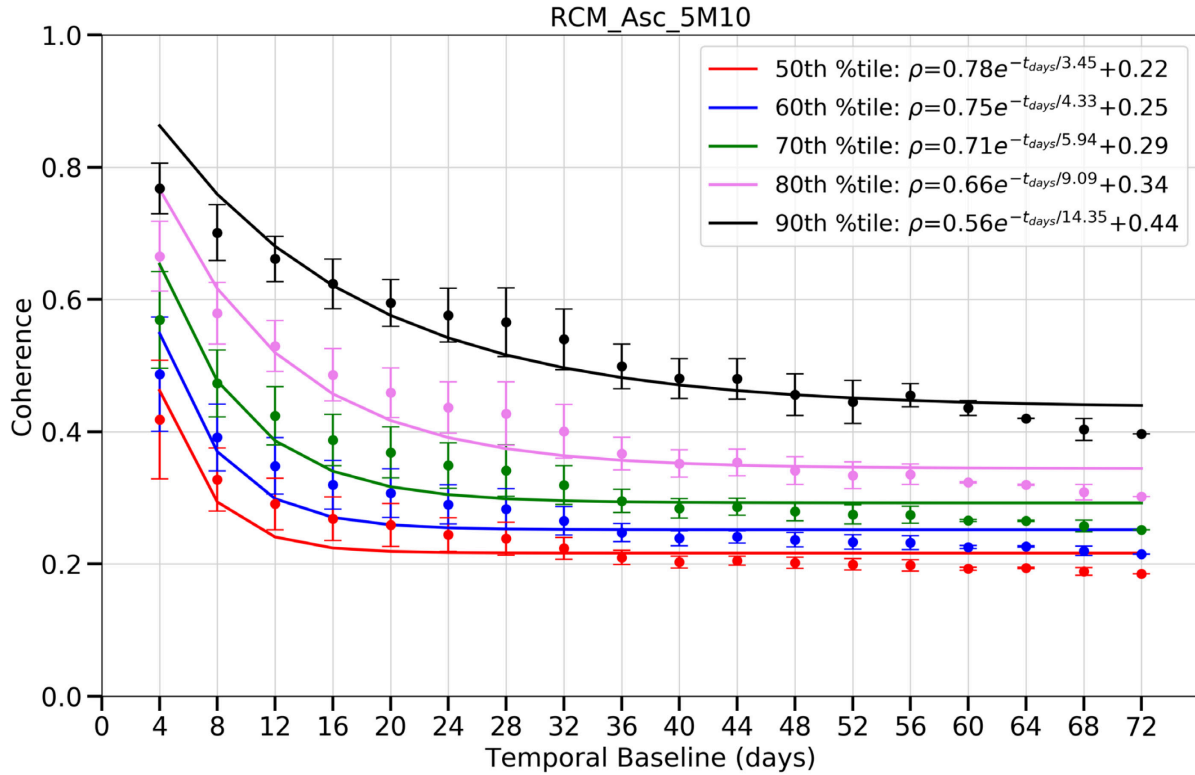


*Figure 4: Coherence decay as a function of temporal baseline. Error bars indicate the mean and standard deviations of all interferograms which share the indicated temporal baseline. Colours represent the spatial coherence percentile with the respective fitted exponential decay models presented in the legend.*
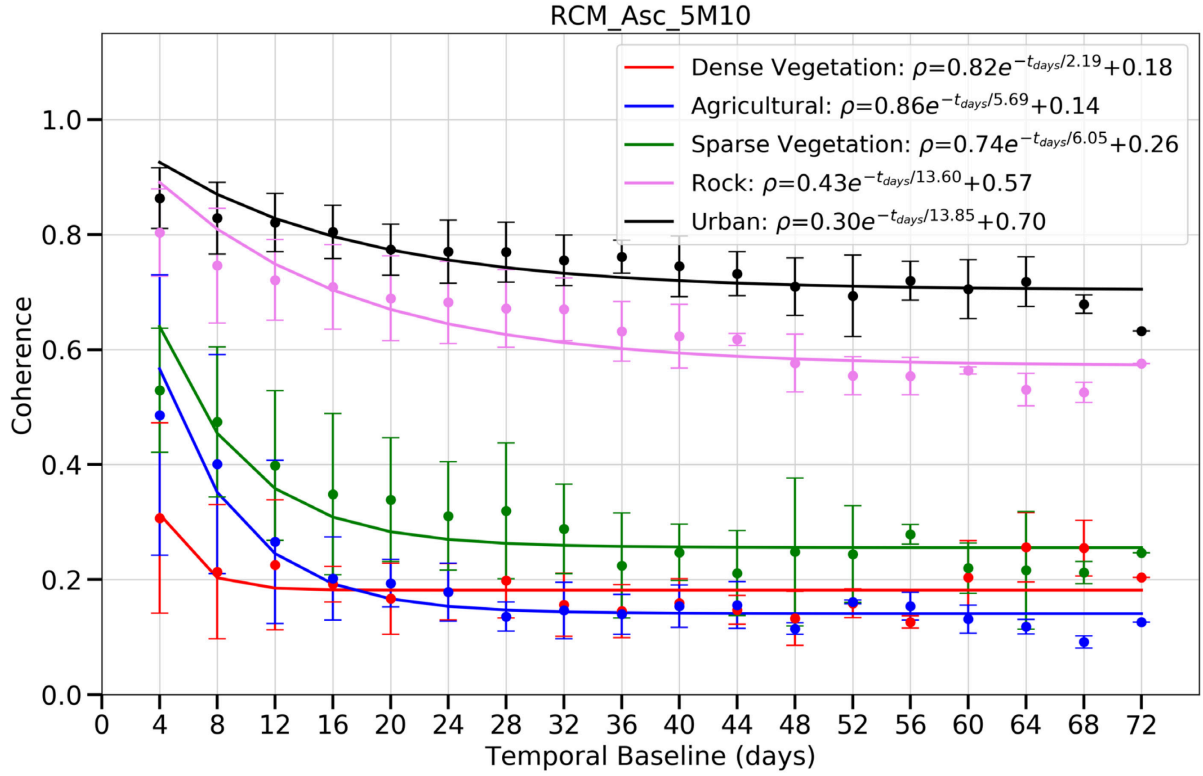
*Figure 5: Coherence decay as a function of temporal baseline and land cover type. Error bars indicate the mean and standard deviations of all interferograms which share the indicated temporal baseline. Colours represent differing land cover types where coherence is measured with the respective fitted exponential decay models presented in the legend.*

In both figures, the exponential decay models provide reasonable fits to the trends in temporal decorrelation. Examination of the trends in Figure 4 shows rapid decreases in coherence as the temporal baseline increases beyond the minimum 4-day repeat of RCM. For pixels in the 50th percentile, the coherence before spatial filtering decreases by 30% (0.42 to 0.29) between interferograms formed between 4-day and 12-day baselines and decreases by 40% (0.42 to 0.24) between interferograms formed between 4-day and 24-day baseline. For pixels in the 90th percentile, the coherence decreases by 14% (0.77 to 0.66) between interferograms formed between 4-day and 12-day baselines and decreases by 25% (0.77 to 0.58) between interferograms formed between 4-day and 24-day baselines.

As described in other works, Figure 5 shows a strong dependence of model parameters with land cover type (Parizzi et al. 2010). Coherence is seen to decrease more rapidly for vegetated and agricultural land cover than for urban and rock land cover. In addition, the urban and rock land cover types show significant residual coherence for large temporal baselines with values of $\rho_0 = 0.70$ and $\rho_0 = 0.57$ respectively. These two land cover types indicate decreases of only 27% and 28% between the coherence of 4-day and 72-day temporal baselines. For the sparse vegetation, dense vegetation and agricultural land cover types, a 50% decrease in coherence is observed at 36, 32, and 16-day temporal baselines when compared with the 4-day coherence.

## 4.2 Radiometric Calibration

For the Thompson River site, the effect of the radiometric calibration on spatial coherence was investigated. Interferograms were generated for the Thompson River site for the six LUTs listed in Table 2.

For the Beta-nought, Sigma-nought, and Gamma-nought LUTs, RCM offers a choice of either 16-bit or 32-bit precision. Floating point LUTs offer a large dynamic range when compared with integer precision, however image sizes are doubled. For RCM data the 16-bit LUTs carry the prefix "Constant" while the 32-bit LUTs carry the prefix "Unity".

The effect of the LUT choice on spatial coherence was tested for the three LUT calibrations for both the 16-bit and 32-bit precisions. To compare the differences, the average spatial coherence for each LUT choice was compared against the mean average across all LUT choices. These results were then grouped by the temporal baseline of the interferograms. The results of this analysis are presented in Figure 6.
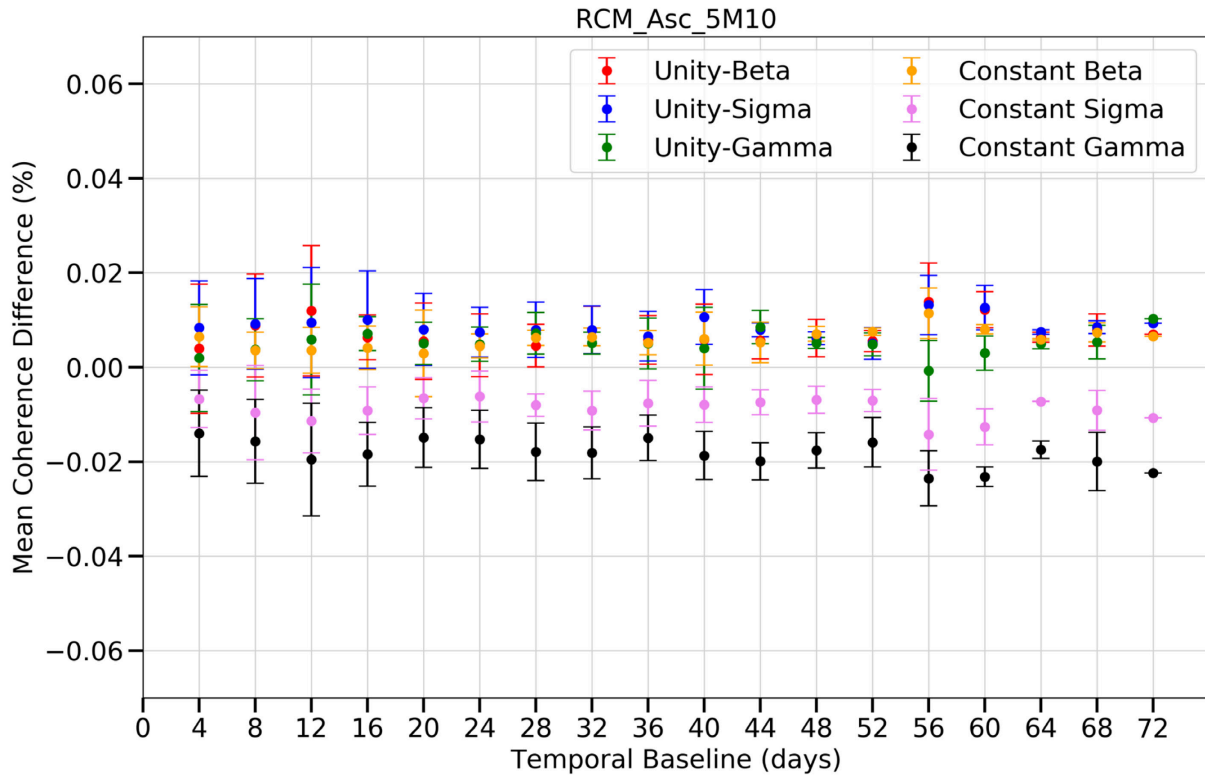


*Figure 6: Average spatial coherence comparison between LUT calibrations. The average spatial coherence for each LUT was compared against the mean average across all LUT calibrations. The prefix "Constant" refers to 16-bit LUT precision while the prefix "Unity" refers to 32-bit precision.*

Figure 6 indicates no significant differences in the measured mean coherence between the 16-bit and 32-bit LUT types. The higher precision 32-bit LUTs show a negligible increase in mean coherence of less than 0.1% when compared with the 16-bit LUTs, indicating that for this test site the higher precision LUT does not increase coherence for distributed targets. However, in a persistent scatterer analysis and for individual targets with high backscatter, the higher precision 32-bit LUT may reduce possible saturation effects.

## 4.3 ScanSAR Interferometry

The capability of RCM ScanSAR data for wide area ground deformation monitoring was tested for the Taal volcano region in the Philippines using the RCM data listed in Table 1. Each ScanSAR scene is comprised of 4 subswaths with a total of 79 bursts. For DInSAR analysis, each burst must be coregistered to a reference burst prior to being integrated into a combined mosaic. Phase preserving techniques must be applied at burst boundaries in an effort to reduce phase discontinuities and ramps (Bamler et al. 1999; Holzner and Bamler 2002). In order to correctly ingest and process RCM interferometric ScanSAR data, the Canada Centre for Remote Sensing (CCRS) worked directly with GAMMA Remote Sensing to test, modify and validate processing software (Wegmuller and Werner 1997).

The results of this work are presented in Figure 7 which shows the MLI with burst boundaries indicated, DEM, and the wrapped interferometric phase and coherence for a 4-day period. Figure 7(a) shows the burst boundaries where phase discontinuities can occur in processing. Inspection of the wrapped phase in Figure 7(c) indicates no phase discontinuities at burst boundaries or a residual phase ramp. For further validation of the ScanSAR processing methodology, a full network of interferograms was created from the available imagery. From the 12 image dates, a total of 66 differential interferograms were created, spatially unwrapped, and converted to LOS displacements. Using MSBAS techniques, the 56-day cumulative displacement was derived and is presented in Figure 8.

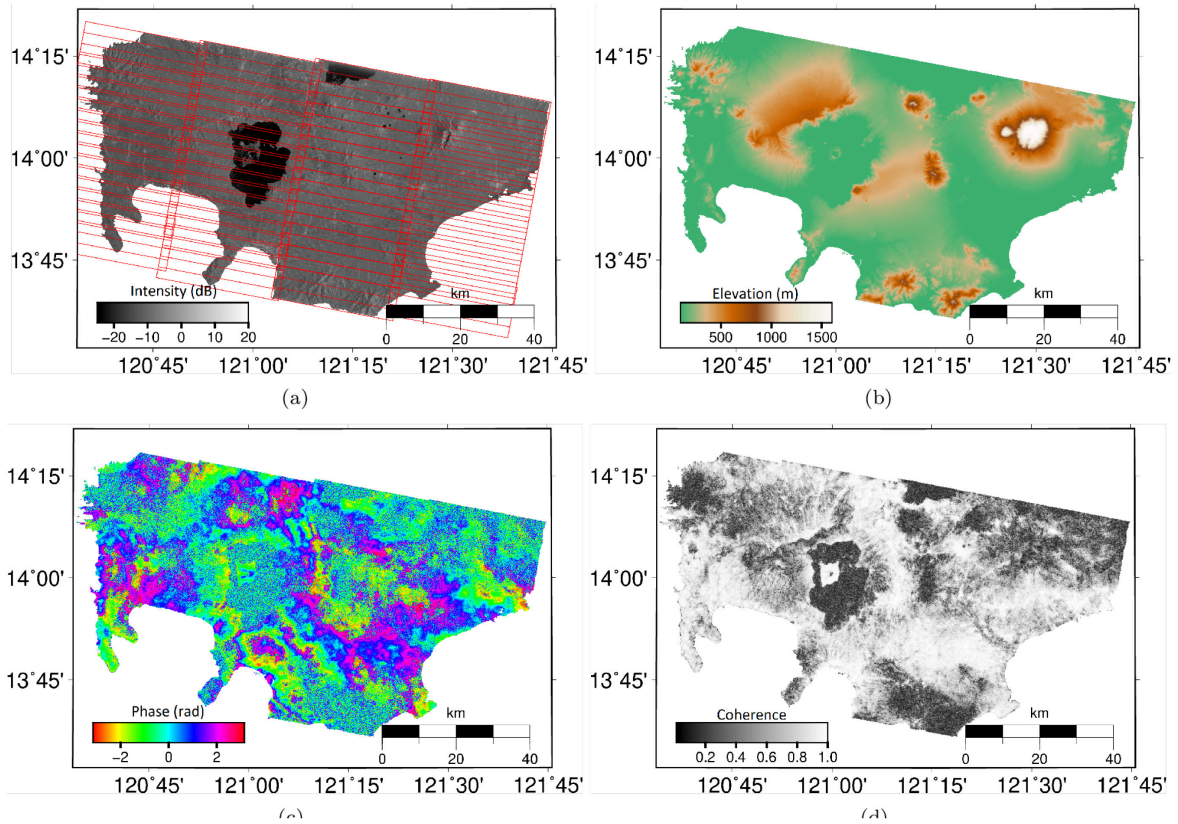*Figure 7: Overview of the ScanSAR analysis region. The average MLI (a) was computed from 12 RCM descending, right-looking SAR images from 2020/03/01 to 2020/04/26. The spatial extents of the 79 ScanSAR bursts are outlined in red. The DEM (b) over the region was obtained from the ASTER GDEM archive. The spatially filtered wrapped phase (c) and coherence (d) for a 4 day period between 2020/04/18 and 2020/04/22.*
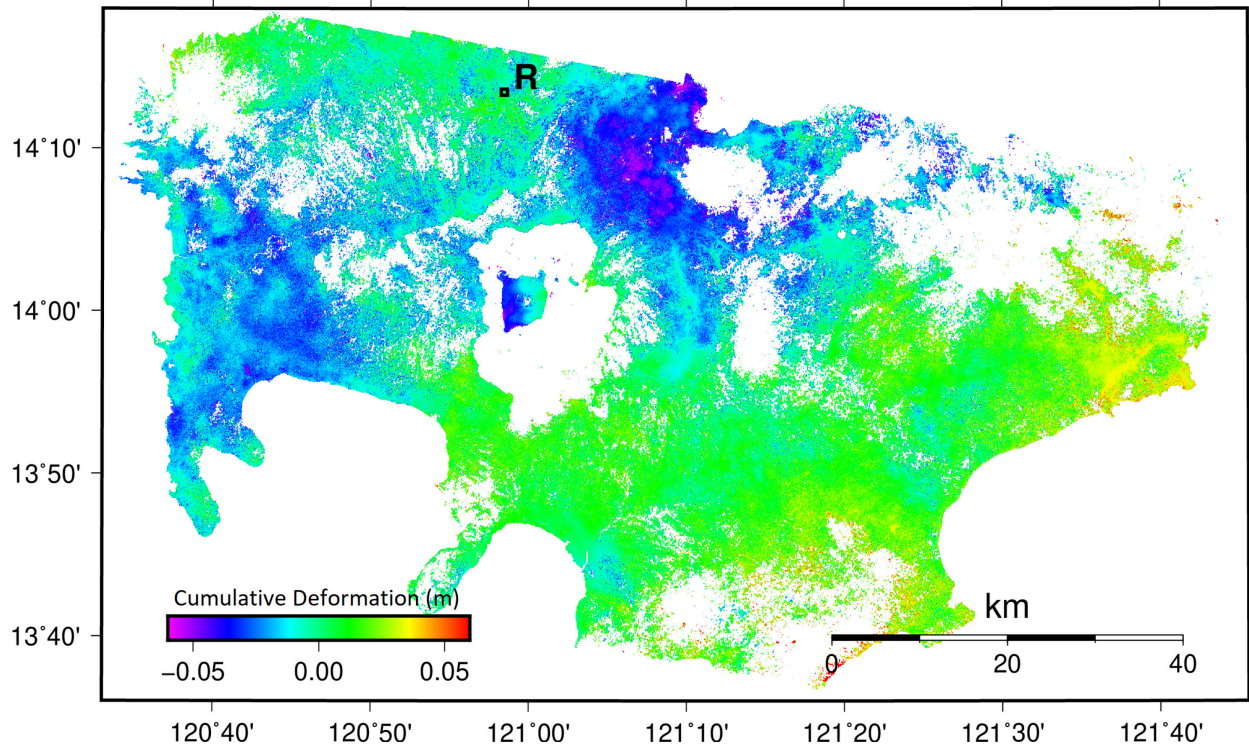
*Figure 8: Cumulative LOS deformation between 2020/03/01 and 2020/04/26 for the ScanSAR analysis region. The stable reference region "R" is automatically selected and is used in the MSBAS algorithm to remove residual phase offsets in the unwrapped interferograms.*

Figure 8 demonstrates a validation of the novel RCM ScanSAR interferometric mode and processing methodology. While residual atmospheric phase appears to be present, there are no indications of phase discontinuities or ramps in the cumulative deformation product. From the cumulative displacement map presented in Figure 8, no significant ground deformation signals are detected during the testing period. Residual atmospheric phase is present as the analysis does not fit and remove atmospheric phase screens. Regions with coherence lower than the filtered coherence threshold of 0.4 are masked out of the displacement map. These regions may represent areas of more rapid land cover change. This example validates the processing and performance of RCM ScanSAR interferometry for wide area ground deformation monitoring, although further refinements would be needed to extract correct values of displacement from this example.

## 4.4 Compact-Pol Interferometry

The performance of the novel RCM CP data for interferometric analysis was tested for the agricultural region near Bassano, Alberta using the RCM data listed in Table 1. Examples of changes in the radar backscatter due to differences in scattering properties for the two combinations of transmit and receive polarizations (CH and CV) are presented in Figure 9. For interferometric analysis, it will be determined whether CP data can be processed to form coherent interferograms as well as to determine whether either combination (CH or CV) demonstrates increased coherence. Examples of the MLI, DEM, and the wrapped interferometric phase and coherence for a 4-day period using the CH polarization are presented in Figure 10.

17
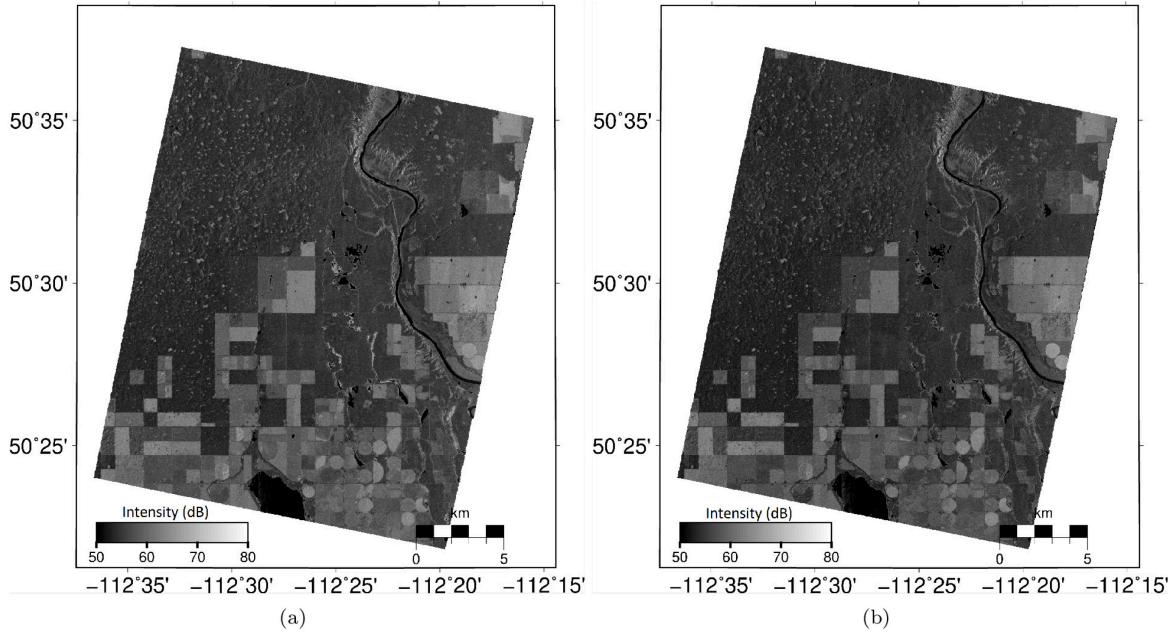
*Figure 9: Comparison of CH (a) and CV (b) average MLI images over the CP test region.*

In Figure 9, variations in the backscatter intensity between the CH and CV polarizations are apparent. The strength of the backscatter signal depends upon factors such as the geometric and electromagnetic properties of the distributed scatterers within the resolution cell. In particular, some agricultural areas display clear differences in intensities and could be used in applications such as crop identification.

*Figure 10: Overview of the RCM CP analysis region. The average MLI (a) was computed from 5 RCM descending, right-looking SAR images f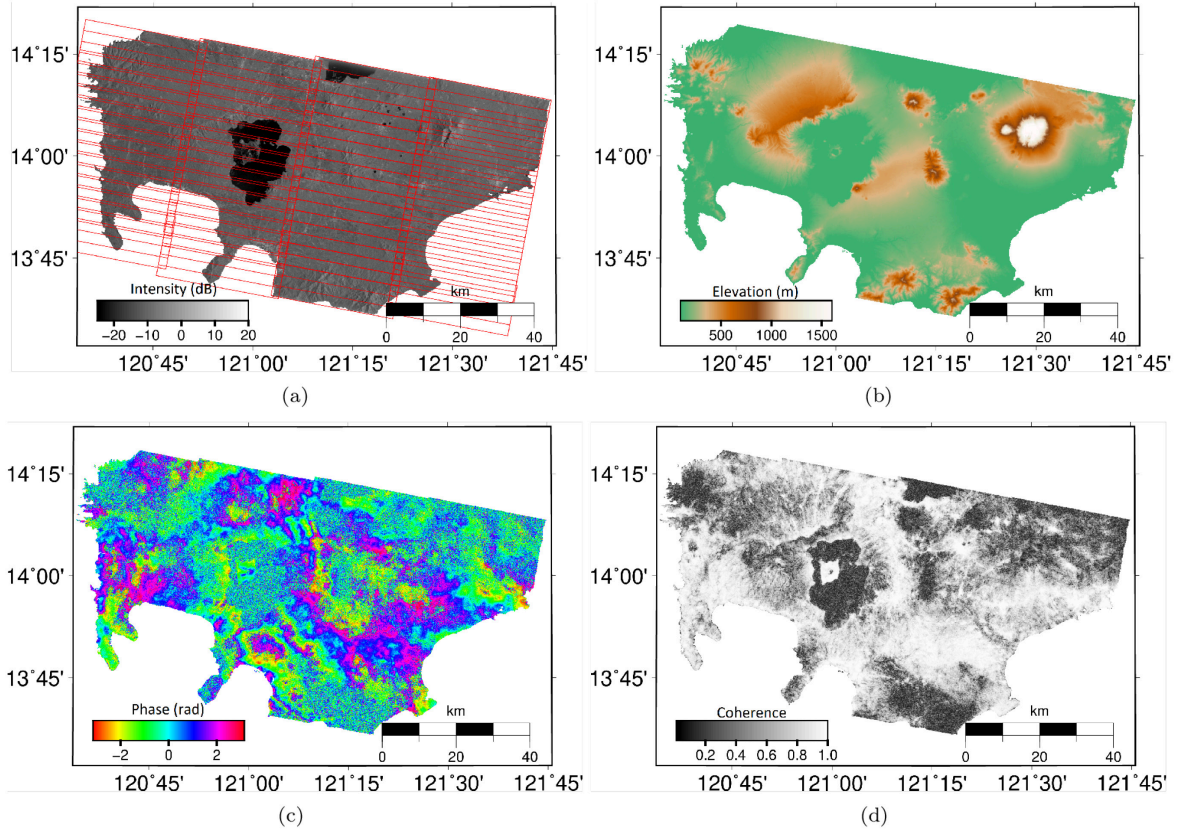rom 2020/06/19 to 2020/08/22. The DEM (b) over the region was obtained from the ASTER GDEM archive. The spatially filtered wrapped phase (c) and coherence (d) for a 4 day period between 2020/07/25 and 2020/7/29 for the CH combination.*

From Figure 10(c) and Figure 10(d), it is apparent that CP data can be successfully processed to form coherent interferograms. Differences in the spatial coherence prior to filtering between the two polarization combinations were measured for 10 interferograms using a 5 pixel by 5 pixel window. The results of this analysis are presented in Table 3. These differences in coherence are also represented visually in histograms for a subset of these interferograms as shown in Figure 11.

*Table 3: Spatial coherence for CH and CV interferometric pairs for the CP dataset.*

| First date | Second date | $\rho_{CH}$ | $\rho_{CV}$ |
|:---:|:---:|:---:|:---:|
| 2020/06/19 | 2020/06/27 | 0.40 | 0.39 |
| 2020/06/19 | 2020/07/25 | 0.31 | 0.30 |
| 2020/06/19 | 2020/07/29 | 0.29 | 0.28 |
| 2020/06/19 | 2020/08/22 | 0.25 | 0.25 |
| 2020/06/27 | 2020/07/25 | 0.37 | 0.36 |
| 2020/06/27 | 2020/07/29 | 0.35 | 0.34 |
| 2020/06/27 | 2020/08/22 | 0.28 | 0.28 |
| 2020/07/25 | 2020/07/29 | 0.59 | 0.57 |

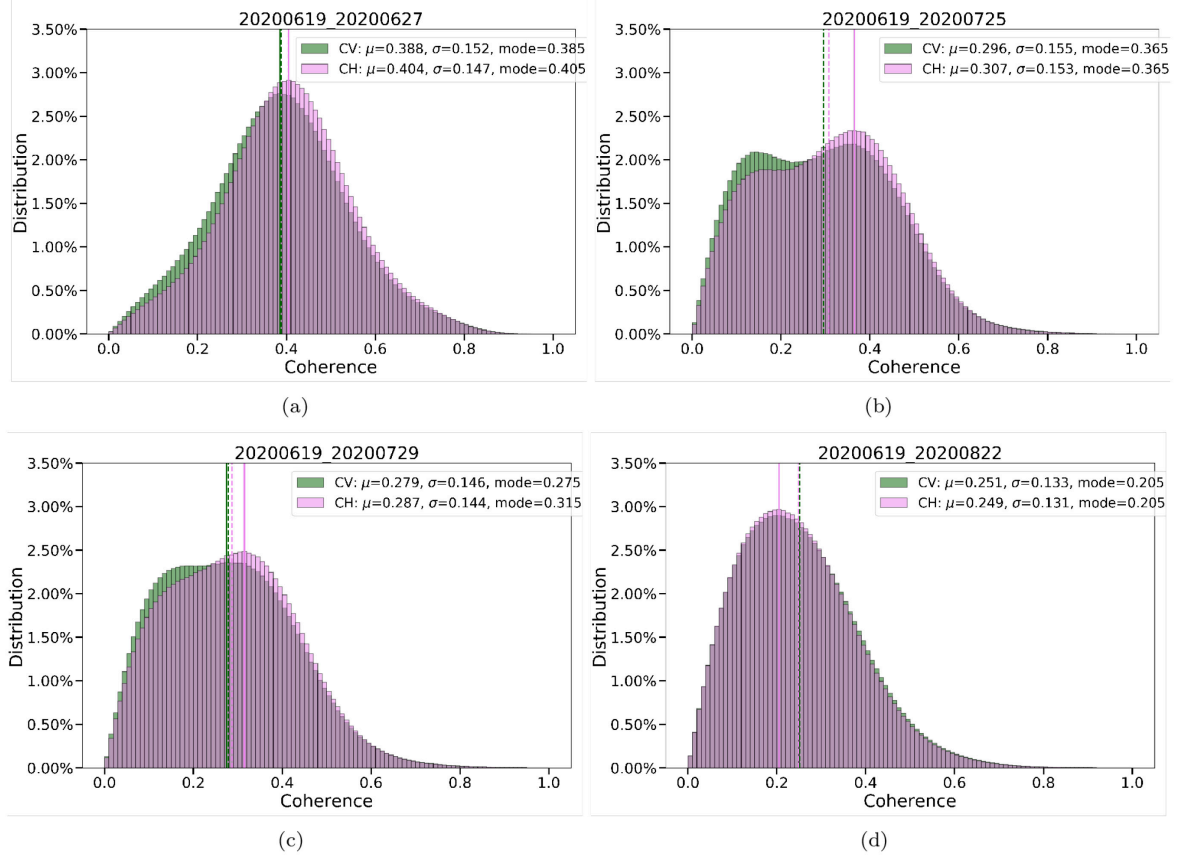| 2020/07/25 | 2020/08/22 | 0.38 | 0.36 |
| 2020/07/29 | 2020/08/22 | 0.45 | 0.43 |



*Figure 111: Comparison of spatial coherence for CH (purple) and CV (green) polarizations for interferograms between 2020/06/19 and 2020/06/27 (a), 2020/06/19 and 2020/07/25 (b), 2020/06/19 and 2020/07/29 (c), 2020/06/19 and 2020/08/22 (d).*

When averaged over all 10 interferometric pairs, the spatial coherence for the CH pairs is $\overline{\rho_{CH}} = 0.37 \pm 0.1$ while $\overline{\rho_{CV}} = 0.36 \pm 0.09$ for the CV pairs. The CH combination shows slightly increased mean coherence, however the variance in the CV pairs is slightly lower when compared with CH. Interestingly, when coherence is low ($\rho < 0.3$), some CV pairs indicate higher spatial coherence than the CH counterpart.

From these results it can be determined that RCM CP data can be used to form coherent interferograms. Coherence differences between the CH and CV combination appear to be minimal but may warrant further investigation.

# 5. Discussion and Conclusions

In this technical note we investigated the DInSAR characteristics of the RCM system with a specific focus on temporal trends in decorrelation, the effect of the radiometric calibration on spatial coherence, and the performance of both wide area ScanSAR and the CP modes for DInSAR ground deformation analysis.

The impact of the high temporal resolution offered by the 4-day repeat cycle of the RCM on temporal decorrelation trends was tested for a region in British Colombia, Canada. The spatial coherence of differential interferograms prior to filtering was measured across numerous temporal baselines. With these measurements, we also created and fit simple models which parameterized the evolution of the temporal decorrelation.

The 4-day repeat pass interval of RCM was shown to provide greatly increased coherence when compared with 12 and 24-day intervals. The temporal evolution of the decorrelation was described by a simple exponential model which showed reasonable agreement for both short and long temporal baselines. The measurements of spatial coherence as a function of temporal baseline as well as the decorrelation models were presented in Figure 4.

Apparent in Figure 4 is the rapid decrease in spatial coherence as the temporal baselines increase. For pixels in the 50th percentile, coherence decreases by approximately half (0.42 to 0.21) between the 4-day and 36-day temporal baselines. For pixels in the 90th percentile, coherence is halved (0.77 to 0.39) when comparing the 4-day and 72-day temporal baselines. These changes in coherence can be important when considering coherence thresholds in DInSAR analysis. When deriving cumulative displacements and rates, a coherence threshold is used to select reliable pixels. For the longer 12-day and 24-day temporal baselines, the reduced coherence values could fall beneath this threshold, rendering these interferograms unusable for DInSAR analysis and potentially precluding a cumulative displacement estimate.

The simple exponential model provides a reasonable approximation of this temporal decorrelation. The model follows the steep initial decline in coherence as the temporal baseline increases. For large temporal baselines, the model asymptotes to a slightly higher residual coherence than that shown by the data. A more complex model may better capture this large temporal baseline behaviour.

In Figure 5 the dependence of temporal decorrelation and model parameters on land cover type are demonstrated. For agricultural and vegetated regions, the coherence decreases rapidly as the temporal baseline increases. For the vegetated regions, the coherence decreases by approximately 40% when comparing interferograms with 4-day and 24-day baselines. For the agricultural region this decrease is more than 60%. In these areas, the 4-day repeat pass interval of RCM may be integral in deriving coherent measurements of ground deformation. For the urban and rock land cover types, the decrease in coherence is less rapid and significant residual coherence is measured even for large temporal baselines. In coherent regions such as these, a 4-day revisit interval may not be necessary for deriving coherent measurements of ground deformation and longer temporal baselines can be employed.

These measurements indicate that DInSAR analyses using RCM data with its shorter 4-day repeat interval can offer increased coherence and thus increased reliability of phase measurements when compared with the longer repeat intervals of other C-band sensors. This may be of particular importance in regions which undergo significant and rapid changes in ground cover such as vegetation and agriculture. This can be particularly impactful for monitoring regions in Canada, where rapid temporal decorrelation may prevent other sensors from measuring meaningful results, rendering RCM a valuable instrument in these areas.

In addition to analyzing the temporal dependence of the spatial coherence, the effect of the radiometric calibration on spatial coherence was also investigated. For the case of distributed targets, three conventional reference areas were examined (Beta-nought, Sigma-nought, and Gamma-nought) to determine if precision of the applied LUT has a significant effect on the measured mean spatial coherence. RCM provides the option for 32-bit precision LUTs, which offers higher precision than traditional 8 and 16-bit LUTs.

The results of the comparison between the measured spatial coherence for different LUT calibrations and precision levels are presented Figure 6. The RCM naming convention denotes 16-bit precision LUTs with the prefix "Constant" and 32-bit precision LUTs with the prefix "Unity". For the Sigma-nought and Gamma-nought calibrations, the measured mean spatial coherence is increased when using the higher precision 32-bit precision LUT. However, the change in mean coherence is less than 0.1%. For use in DInSAR analysis, the 32-bit precision LUTs do not appear to significantly improve the quality of the interferometric results in this distributed scatterer example. However, for the purposes of building consistency across the RCM SAR catalog, as well as to enable diverse application of RCM SAR data, it is suggested that the Unity-beta LUT be employed when ordering new RCM SAR acquisitions.

For wide area ground deformation monitoring, the RCM ScanSAR mode was investigated and found to produce coherent results across a 125 km swath width with no apparent phase discontinuities or ramps. The 30 m spatial resolution and 4-day temporal resolution of this ScanSAR mode was found to be compatible with monitoring and measuring larger scale ground deformation patterns such as landslides, seismic events, and volcanic activity. From the connected network of 66 interferograms, a 56 day cumulative LOS displacement was derived and presented in Figure 8. This study demonstrates that the burst synchronization of RCM ScanSAR data required for DInSAR analysis is well maintained over time, allowing for the production of cumulative displacements and time series results. A cumulative displacement measurement was presented as a practical example of wide area monitoring. With this example, no significant ground deformation signals were detected. Some larger scale deformation patterns may be due to changes in ground cover or residual atmospheric noise. More heavily vegetated regions and some mountainous terrain undergo temporal decorrelation and are masked out of the cumulative result. This example illustrates the potential and utility of the RCM ScanSAR mode for wide area monitoring of ground deformation.

Lastly, the use of the novel RCM CP mode for interferometric analysis was investigated. Here it was found that both the CH and CV polarizations formed coherent interferograms with the CH combination showing slightly higher mean coherence. The spatial coherence for all of the

interferometric pairs is listed in Table 3 with a subset presented visually as histograms in Figure 11.

When performing DInSAR analysis with CP data, the use of the CH mode is recommended due to its higher measured coherence. However, both the CH and CV mode were shown to provide data which is compatible with coherent interferometric analysis. This allows for the potential to perform parallel analyses using CP data for both polarimetric analysis of properties such as soil moisture and crop identification as well as interferometric analysis of properties such as ground deformation or change detection.

In summary, we assessed four novel aspects of the SAR interferometric performance of the RCM system. Trends in temporal decorrelation were investigated through the measured interferometric spatial coherence for varying temporal baselines. The shorter 4-day temporal baselines offered by RCM were found to yield increased spatial coherence when compared with the 12 and 24-day temporal baselines offered by other individual C-band sensors. The temporal dependence of the coherence decay was found to be consistent with an exponential decay model. The effect of the precision of the radiometric calibration for distributed targets was found to have negligible influence on the measured spatial coherence for the investigated region of interest. Both the novel RCM ScanSAR and CP modes were tested and provided coherent results in interferometric analyses.

## 6. Acknowledgements

# 7. References

Aimaiti, Yusupujiang, Fumio Yamazaki,Wen Liu, and Alimujiang Kasimu. 2017. Monitoring of Land-Surface Deformation in the Karamay Oilfield, Xinjiang, China, Using SAR Interferometry. Applied Sciences 7(8). doi:10.3390/app7080772.

Bamler, R., D. Geudtner, B. Schattler, P.W. Vachon, U. Steinbrecher, J. Holzner, J. Mittermayer, H. Breit, and A. Moreira. 1999.
RADARSAT ScanSAR interferometry. In IEEE 1999 International Geoscience and Remote Sensing Symposium. IGARSS'99 (Cat.No.99CH36293), Volume 3, pp. 1517–1521 vol.3. doi:10.1109/IGARSS.1999.772005.

Bato, M. G., P. Lundgren, V. Pinel, R. Solidum Jr., A. Daag, and M. Cahulogan. 2021. The 2020 Eruption and Large Lateral Dike Emplacement at Taal Volcano, Philippines: Insights From Satellite Radar Data. Geophysical Research Letters 48(7), e2021GL092803.doi:https://doi.org/10.1029/2021GL092803.

Berger, Michael, Jose Moreno, Johnny A. Johannessen, Pieternel F. Levelt, and Ramon F. Hanssen. 2012. ESA's sentinel missions in support of Earth system science. Remote Sensing of Environment 120, 84–90. The Sentinel Missions - New Opportunities for Science, doi:https://doi.org/10.1016/j.rse.2011.07.023.

Brisco, Brian, Masoud Mahdianpari, and Fariba Mohammadimanesh. 2020. Hybrid Compact Polarimetric SAR for Environmental Monitoring with the RADARSAT Constellation Mission. Remote Sensing 12(20). doi:10.3390/rs12203283.

Brisco, Brian, Kevin Murnaghan, Shimon Wdowinski, and Sang-Hoon Hong. 2015. Evaluation of RADARSAT-2 Acquisition Modes for Wetland Monitoring Applications. Canadian Journal of Remote Sensing 41(5), 431–439. doi:10.1080/07038992.2015.1104636.

Canadian Space Agency. 2019. Mission milestones. https://www.asc-csa.gc.ca/eng/satellites/radarsat/updates.asp.

Canaslan Çomut, Fatma and Aydın Üstün. 2012. Impact of Perpendicular and Temporal Baseline Characteristics on InSAR Coherence Maps. In Proc. FIG Working Week.

Charbonneau, François, B. Brisco, Russell Raney, Heather McNairn, C. Liu, P. Vachon, Jiali Shang, R. DeAbreu, Catherine Champagne, A. Merzouki, and Torsten Geldsetzer. 2010. Compact Polarimetry Overview and Applications Assessment. Canadian Journal of Remote Sensing 36, 298–. doi:10.5589/m10-062.

Cloude, S. R. and K. P. Papathanassiou. 1998. Polarimetric SAR interferometry. IEEE Transactions on Geoscience and Remote Sensing 36(5), 1551–1565. doi:10.1109/36.718859.

Costantini, M. 1998. A novel phase unwrapping method based on network programming. IEEE Transactions on Geoscience and Remote Sensing 36(3), 813–821

Côté, Stéphane, Mélanie Lapointe, Eric Arsenault, Magdalena Wierus, and Steve Iris. 2019. RADARSAT Constellation Mission. In CEOS SAR 2019 Workshop VH-RODA Workshop, Canadian Space Agency, Longueuil, Canada. https://earth.esa.int/documents/700255/4038563/8+RADARSAT+Constellation+Mission_CEOS SARWGCV-VHRODA+v4.pdf.

Dabboor, Mohammed, Suman Singha, Benoit Montpetit, Benjamin Deschamps, and Dean Flett. 2019. Pre-Launch Assessment of RADARSAT Constellation Mission Medium Resolution Modes for Sea Oil Slicks and Lookalike Discrimination. Canadian Journal of Remote Sensing 45(3-4), 530–549. doi:10.1080/07038992.2019.1659722.

Davidson, Malcolm, Paul Snoeij, Evert Attema, Björn Rommen, Nicolas Floury, Guido Levrini, and Berthyl Duesmann. 2010, 07. Sentinel-1 Mission Overview. Volume 1, pp. 1 – 4. doi:10.1109/IGARSS.2009.5416921.

De Abreu, R., M. Arkett, A. Cheng, T. Zagon, D. Mueller, P.W. Vachon, and J.Wolfe. 2011. RADARSAT-2 mode selection for maritime surveillance. Defence Research and Development Canada. External Client Report, 185.

Delos Reyes, Perla J., Ma. Antonia V. Bornas, Dale Dominey-Howes, Abigail C. Pidlaoan, Christina R. Magill, and Renato U. Solidum, Jr. 2018. A synthesis and review of historical eruptions at Taal Volcano, Southern Luzon, Philippines. Earth-Science Reviews 177, 565–588. doi:https://doi.org/10.1016/j.earscirev.2017.11.014.

Dudley, J. and S. Samsonov. 2020. The Government of Canada automated processing system for change detection and ground deformation analysis from RADARSAT-2 and RADARSAT Constellation Mission Synthetic Aperture Radar data: description and user guide. Geomatics Canada, Open File 63. doi:10.4095/327790.

Engelbrecht, J., C. Musekiwa, J. Kemp, and M. R. Inggs. 2014. Parameters Affecting Interferometric Coherence—The Case of a Dynamic Agricultural Region. IEEE Transactions on Geoscience and Remote Sensing 52(3), 1572–1582. doi:10.1109/TGRS.2013.2252620.

Feng, W., Z. Li, T. Hoey, Y. Zhang, R. Wang, S. Samsonov, Y. Li, and Z. Xu. 2014. Patterns and mechanisms of coseismic and postseismic slips of the 2011 MW 7.1 Van (Turkey) earthquake revealed by multi-platform synthetic aperture radar interferometry. Tectonophysics 632, 188–198. doi:10.1016/j.tecto.2014.06.011.

Feng, W., E. Lindsey, S. Barbot, S. V. Samsonov, K. Li, P. Li, Z. Li, R. Almeida, J. Chen, and X. Xu. 2016. Source characteristics of the 2015 MW 7.8 Gorkha earthquake and its MW 7.2 aftershock from space geodesy. Tectonophysics. doi:10.1016/j.tecto.2016.02.029.

Ferretti, Alessandro, Carlo Colesanti, Daniele Perissin, Claudio Prati, and Fabio Rocca. 2003. Evaluating the effect of the observation time on the distribution of SAR permanent scatterers. FRINGE 2003 Workshop. ESA Special Publication 550,26.

Ferretti, A., C. Prati, and F. Rocca. 2001. Permanent scatterers in SAR interferometry. IEEE Transactions on Geoscience and Remote Sensing 39, 8–20.

Goldstein, R. and C.Werner. 1998. Radar interferogram filtering for geophysical applications. Geophysical Research Letters 25(21), 4035–4038.

Hamling, I. J., E. D'Anastasio, L. M. Wallace, S. Ellis, M. Motagh, S. Samsonov, N. Palmer, and S. Hreinsdóttir. 2014. Crustal deformation and stress transfer during a propagating earthquake sequence: The 2013 Cook Strait sequence, central New Zealand. Journal of Geophysical Research: Solid Earth 119(7), 6080–6092. doi:https://doi.org/10.1002/2014JB011084.

Holzner, Jürgen and Richard Bamler. 2002. Burst-mode and ScanSAR interferometry., IEEE Transactions on Geoscience and Remote Sensing 40, 1917 – 1934. doi:10.1109/TGRS.2002.803848.

Huntley, D., D. Rotheram-Clarke, A. Pon, A. Tomaszewicz, J. Leighton, R. Cocking, and J. Joseph. 2021. Benchmarked RADARSAT-2, SENTINEL-1 and RADARSAT Constellation Mission Change-Detection Monitoring at North Slide, Thompson River Valley, British Columbia: ensuring a Landslide-Resilient National Railway Network. Canadian Journal of Remote Sensing. doi:10.1080/07038992.2021.1937968.

Imhoff, Marc. 1995. Radar backscatter and biomass saturation: Ramification for global biomass inventory. Geoscience and Remote Sensing, IEEE Transactions on Geoscience and Remote Sensing, vol. 33, no. 2, pp. 511-518, March 1995, doi: 10.1109/TGRS.1995.8746034. .

Journault, Jeff, Renato Macciotta, Michael Hendry, François Charbonneau, David Huntley, and Peter Bobrowsky. 2017. Measuring displacements of the Thompson River valley landslides, south of Ashcroft, BC, Canada, using satellite InSAR. Landslides. doi:10.1007/s10346-017-0900-1.

Lehrbass, B., S. Samsonov, J. Dudley, N. Svacina, H. Drouin, V. Decker, and S. Tolszczuk-Leclrec. 2021. Emergency Geomatics Service activation for Turtle Mountain, Alberta InSAR monitoring. Geomatics Canada, Open File 64. doi:10.4095/328268.

Liang, Cunren, Qiming Zeng, Jianying Jia, Jian Jiao, and Xi'ai Cui. 2013. ScanSAR interferometric processing using existing standard InSAR software for measuring large scale land deformation. Computers & Geosciences 51, 439–448. doi:https://doi.org/10.1016/j.cageo.2012.08.011.

Livingstone, C., I. Sikaneta, C. Gierull, S. Chiu, and P. Beaulne. 2006. RADARSAT-2 System and Mode Description. In Proceedings of RTO-MP-SCI-150, paper 15, Neuilly-sur-Seine, France.

Lundgren, P., S.V. Samsonov, C.M. Lõpez Velez, and M. Ordoñez. 2015. Deep source model for Nevado del Ruiz Volcano, Colombia, constrained by interferometric synthetic aperture radar observations. Geophysical Research Letters 42(12), 4816–4823. doi:10.1002/2015GL063858.

McNairn, H., A. Merzouki, Y. Li, G. Lampropoulos, W. Tan, J. Powers, and M. Friesen. 2018. Retrieval of Field-Scale Soil Moisture Using Compact Polarimetry: Preparing for the Radarsat-Constellation. In IGARSS 2018 - 2018 IEEE International Geoscience and Remote Sensing Symposium, pp. 6135–6138. doi:10.1109/IGARSS.2018.8518980.

MDA Systems Ltd. 2020. RADARSAT Constellation Mission Product Specification, Contract report for Canadian Space Agency. Technical Report RCM-SP-52-9092, MDA Systems Ltd. 30 p.

MDA Technical Staff. 2016. RADARSAT-2 Application Look-Up Tables (LUTs). Technical report. https://mdacorporation.com/docs/default-source/technical-documents/geospatial-services/radarsat-2-application-look-up-tables.pdf.

Miranda, Nuno and P.J. Meadows. 2015. Radiometric Calibration of S-1 Level-1 Products Generated by the S-1 IPF. ESA Technical Note. ESA-EOPG-CSCOP-TN-0002. https://sentinel.esa.int/documents/247904/685163/S1-Radiometric-Calibration-V1.0.pdf

Morales, Anieri, Falk Amelung, and Rodrigo Eco. 2015. Volcano Deformation and Modeling on Active Volcanoes in the Philippines from ALOS InSAR Time Series. FRINGE 2015. ESA Special Publication 731,doi:10.5270/Fringe2015.pp302.

Morena, L C, K V James, and J. Beck. 2004. An introduction to the RADARSAT-2 mission. Canadian Journal of Remote Sensing 30(3), 221–234. doi:10.5589/m04-004.

Parizzi, Alessandro, Xiao Ying Cong, and Michael Eineder. 2010, March. First Results from Multifrequency Interferometry. A Comparison of Different Decorrelation Time Constants at L, C and X Band. In H. Lacoste (Ed.), ESA Special Publication, Volume 677 of ESA Special Publication, pp. 5.

Pearse, J., V. Singhroy, S. Samsonov, and J. Li. 2014. Anomalous surface heave induced by enhanced oil recovery in northern Alberta: InSAR observations and numerical modeling. Journal of Geophysical Research. doi:10.1002/2013JB010885.

Preiss, M. and N.J.S. Stacy. 2006. Coherent change detection: theoretical description and experimental results. pp. 116. Defence Science and Technology Organisation (Australia) Intelligence Surveillance and Reconnaissance Division. DSTO-TR-1851.

Raney, R. Keith. 2019. Hybrid Dual-Polarization Synthetic Aperture Radar. Remote Sensing 11(13). doi:10.3390/rs11131521.

Samsonov, S.V., M. Czarnogorska, and F. Charbonneau. 2015. Selecting optimal RADARSAT Constellation Mission beams for monitoring ground deformation in Alberta's oil sands. Canadian Journal of Remote Sensing 41(5), 390–400. doi:10.1080/07038992.2015.1104632.

Samsonov, S.V. and N. d'Oreye. 2017. Multidimensional Small Baseline Subset (MSBAS) for Two-Dimensional Deformation Analysis: Case Study Mexico City. Canadian Journal of Remote Sensing 43(4). doi:10.1080/07038992.2017.1344926.

Samsonov, S., W. Feng, P. Peltier, H. Geirsson, N. d'Oreye, and K. Tiampo. 2016. Multidimensional Small Baseline Subset (MSBAS) for volcano monitoring in two dimensions: opportunities and challenges. Case study Piton de la Fournaise volcano. Journal of Volcanology and Geothermal Research 344. doi:10.1016/j.jvolgeores.2017.04.017

Samsonov, S.V., W. Feng, and N. Short. 2017. DInSAR products and applications for the RADARSAT Constellation Mission. Geomatics Canada, Open File 37. doi:10.4095/305958.

Singhroy, Vernon, Junhua Li, and François Charbonneau. 2015. High Resolution Rapid Revisit InSAR Monitoring of Surface Deformation. Canadian Journal of Remote Sensing 41(5), 458–472. doi:10.1080/07038992.2015.1104638.

Small, D. 2011. Flattening Gamma: Radiometric Terrain Correction for SAR Imagery. IEEE Transactions on Geoscience and Remote Sensing 49(8), 3081–3093. doi:10.1109/TGRS.2011.2120616.

Small, David, Nuno Miranda, and Erich Meier. 2009. A Revised Radiometric Normalisation Standard for SAR. 2009 IEEE International Geoscience and Remote Sensing Symposium, 2009, pp. IV-566-IV-569, doi: 10.1109/IGARSS.2009.5417439.

Thompson, A. A. 2010. Innovative Capabilities of the RADARSAT Constellation Mission. In 8th European Conference on Synthetic Aperture Radar. 8th European Conference on Synthetic Aperture Radar, 2010, pp. 1-3.

Thompson, Alan A. 2015. Overview of the RADARSAT Constellation Mission. Canadian Journal of Remote Sensing 41(5), 401–407. doi:10.1080/07038992.2015.1104633.

Touzi, R. 1999. Coherence estimation for SAR imagery. IEEE Transactions on Geoscience and Remote Sensing 37(1), 135–149.

Wegmuller, U. and C. Werner. 1997. GAMMA SAR processor and interferometry software. In The 3rd ERS symposium on space at the service of our environment, Florence, Italy.

Yamaguchi, Y., A. B. Kahle, H. Tsu, T. Kawakami, and M. Pniel. 1998. Overview of Advanced Spaceborne Thermal Emission and Reflection Radiometer (ASTER). IEEE Transactions on Geoscience and Remote Sensing 36(4), 1062–1071. doi:10.1109/36.700991.

Zhou, Zhiwei, Zhenhong Li, Susan Waldron, and Akiko Tanaka. 2019. InSAR Time Series Analysis of L-Band Data for Understanding Tropical Peatland Degradation and Restoration. Remote Sensing 11(21). doi:10.3390/rs11212592.